iScience

CellPress
OPEN ACCESS

Article

Visualizing thermal distribution through hydrogel confined ionic system

Qinyuan Gui, Bin Fu, Yonglin He, Shanzhi Lyu, Yingchao Ma, Yapei Wang

yapeiwang@ruc.edu.cn

HIGHLIGHTS

Thermal field distribution can be visualized without professional apparatus

The LCST of ionic liquid can be finely tuned

The mechanism of the LCST adjustment is studied

A fire warning system is established to reduce the threat of fire hazard

Gui et al., iScience *24*, 102085
February 19, 2021
https://doi.org/10.1016/j.isci.2021.102085

iScience

CellPress
OPEN ACCESS

Article

Visualizing thermal distribution through hydrogel confined ionic system

Qinyuan Gui,[1] Bin Fu,[1] Yonglin He,[1] Shanzhi Lyu,[1] Yingchao Ma,[1] and Yapei Wang[1,2,*]

SUMMARY

Effective thermal regulation has shown great impacts on tremendous aspects of our life and manufacture. However, the invisible nature of thermal field brings us inconvenience or even security hazard. Herein, we present a method to visualize thermal distribution with the aid of a thermally active material. An ionic liquid with lower critical solution temperature is mixed within hydrogel to demonstrate a hydrogel confined ionic system (HCIS). This particular system turns turbid as the temperature exceeds an established temperature threshold, which is adjustable through applying different concentrations of HCl or NaCl. The system offers straightforward images of the spatial thermal distribution whether simple or sophisticated, which is fully in line with computational simulation. The system is further demonstrated with great promise for the application in fire warning to lower the threat induced by electrical failure. The HCIS opens a practical avenue to visualize thermal distribution and improve our thermal regulation efficiency.

INTRODUCTION

Thermal energy, one of the most primitive yet essential kinds of energy, plays a vital role in the evolution course of our civilization. From the wild age to the modern era, human beings have gained increasingly efficient and precise mastery to thermal energy (Wang et al., 2020; Lyu et al., 2019; Shchukina et al., 2018; Zhou et al., 2016, 2020). However, for millions of years, no one has witnessed thermal energy without the assistance of professional apparatuses. Infrared imager is the most commonly used apparatus to visualize thermal field distribution in the fields of industrial manufacture, health service (He et al., 2018), electronic design (Gui et al., 2017), and thermal engineering. It provides us with abundant information to help analyzing and regulating thermal energy. Nevertheless, the infrared imager provides only two-dimensional thermal information (Tao et al., 2017). Real-time 3D imaging of the thermal distribution of an object would be unrealizable. Some important machines, engines for example, have high requirements for spatiotemporal temperature control. It is ideally useful to acquire thermal information from different axes to evaluate their security and efficiency. It would be challenging for infrared imager to fulfill this mission. Another fatal drawback of infrared imager is the limited penetration depth of the infrared light (Cao et al., 2017). For the petrochemical industries, most equipment operating at high temperature and pressure is isolated in a dedicated space, which causes dangers to the entered operators. The thermal distribution within this dedicated space is difficult to be monitored by infrared imager, even though watch windows on the isolating wall are made of transparent glasses. Furthermore, the cumbersome and expensive characters of infrared imager greatly limit its availability to a broader area. For example, the thermal conditions of the instruments and circuits in factories should be monitored frequently to eliminate the threats and thereby ensure the production safety. Such a job is practically accomplished by workers who have to hold infrared imagers and patrol the production rooms constantly. This strategy is time consuming, is of high cost, and also encountered with the possibilities of losing real-time information in a long-term period. Therefore, a new thermal imaging system is worth establishing to compensate the deficiencies of infrared imager, and it is expected to own the following features: (1) presenting the real-time 3D thermal distribution of an object, (2) adjustable thermal imaging range to adapt to particular requirements, and (3) cheap and eco-friendly.

Over the past decades, a subclass of molten salts called ionic liquids (ILs) has received unprecedented attentions and becomes one of the most intensively investigated soft materials (Yang et al., 2018a; Wang et al., 2016; Ota et al., 2014; He et al., 2015). Among them, some thermal-responsive species possess different solubility in other solvents with the variation of temperature, and the phase separation

[1]Department of Chemistry, Renmin University of China, Beijing 100872, China

[2]Lead contact

*Correspondence: yapeiwang@ruc.edu.cn

https://doi.org/10.1016/j.isci.2021.102085

temperature is defined as critical solution temperature (Ueki et al., 2011; Qiao et al., 2017). For the system which possesses lower critical solution temperature (LCST), the solubility of IL in a solvent decreases with the increasing temperature and phase separation occurs above LCST (Fukumoto and Ohno, 2007; Gao et al., 2017; Kohno et al., 2012; Men et al., 2013; Ziolkowski and Diamond, 2013). This abnormal phenomenon has been investigated for years, and the critical temperature was found adjustable (Men et al., 2012; Li et al., 2019a; Choi and Yethiraj, 2015), which appears to be ideally suitable for the thermal visualization. However, the mixture of ionic liquid and solvent is hardly freestanding, making it scarcely possible to attach to the surface of an object (Matsumoto and Endo, 2008; Gao et al., 2019; Wang, 2020; Zhou et al., 2019). An encapsulating container is essentially needed to confine the mixture of IL and solvent in a specific region which goes against rapid thermal transmission and also meets the leakage problem (Chen et al., 2018; Yang et al., 2018b; Lu et al., 2019; Zhao et al., 2020a, 2020b).

Herein, we present a general yet effective method hopefully to offset the inconvenience of the infrared imager. This new thermal imaging method is based on the reversible phase separation of a hydrogel confined ionic system (HCIS). Concretely, a thermal-responsive ionic liquid, tetrabutylphosphonium p-styrenesulfonate ([P_{4444}][SS]), was dissolved in a gelatin network to form a transparent and freestanding hydrogel at room temperature (Zhang et al., 2015). As a result of the phase separation between ionic liquid and hydrogel matrix, optical turbidity specifically occurred in the regions where the local temperature exceeded LCST (Yu et al., 2020; Li et al., 2019b; Alf et al., 2011). Most pointedly, the LCST could be finely tuned to the desired values so as to satisfy programmable thermal imaging with demands on varied thermal thresholds. Several practical attempts demonstrated the great potentials of HCIS to vividly visualize spatial thermal distribution in sophisticated circumstances, which is especially useful for building low-cost and timely fire warning systems.

RESULTS

Preparation and LCST behavior in hydrogel confined ionic system

The ionic liquid was synthetized through an ionic exchange reaction between tetra-n-butylphosphonium bromide ([P_{4444}]Br) and sodium p-styrenesulfonate (Na[SS]) (Figure 1A). Typically, the ionic complex dissolved in the aqueous medium was repeatedly extracted by dichloromethane, driving the formation of target ionic liquid of [P_{4444}][SS] and transferring them into oil phase. Pure [P_{4444}][SS] was obtained after the removal of dichloromethane, which was successfully verified by ^{1}H NMR spectrometer (Figure S1). To obtain the hydrogel confined ionic system (HCIS), [P_{4444}][SS] was mixed with 10 wt.% gelatin solution which was subsequently cross-linked by glutaraldehyde to confine [P_{4444}][SS] in the hydrogel network. Notably, the HCIS before fully cross-linked could be molded into freestanding samples with controlled size and shapes. As exemplified in Figures 1B, a 25 × 25 cm^2 square film was readily prepared by laminating the HCIS between two glass plates. The film was freestanding in a photo frame. At room temperature, it was highly transparent to visible light, and an azalea could be clearly seen through it. When a human hand warmed the HCIS film, the region touched by the hand became turbid and the azalea was obscured accordingly. It was proposed that the hand temperature had been above LCST, which caused the lower solubility of [P_{4444}][SS] within the hydrogel network. As a result, the separated ionic liquid droplets scattered the incident light which accounted for the appearance of opacity.

LCST adjustment in the [P_{4444}][SS]-H_2O binary system

The mole ratio between [P_{4444}][SS] and water content in the hydrogel decides the phase separation temperature, referring to LCST (the phase diagram in Figure 1B). In order to better understand the phenomenon of phase separation in HCIS, insights were provided into the occurrence of LCST in a [P_{4444}][SS]-H_2O binary system. Setting the mole ratio between [P_{4444}][SS] and water at 1:300, phase separation between [P_{4444}][SS] and water occurred at temperature above 40°C. Obviously, under temperature below 40°C, the solution is clear and transparent. When the temperature rises above 40°C, the solvated ionic liquid separates from the solution and aggregates into tiny droplets. As recorded by UV-vis spectrometer, the solution transmittance is reduced from 99.0% to 0.4% (Figure 2A). The solution fully recovers transparent again once it is cooled to room temperature.

The LCST of [P_{4444}][SS] aqueous solution could be finely tuned via the addition of hydrochloric acid (HCl) or sodium chloride (NaCl), in addition to changing the [P_{4444}][SS] concentration. The easy regulation of LCST offers HCIS with great promises for programmable thermal imaging in different application scenarios. Intriguingly, HCl and NaCl exhibit opposite regulation to the critical temperature of [P_{4444}][SS]. With raising

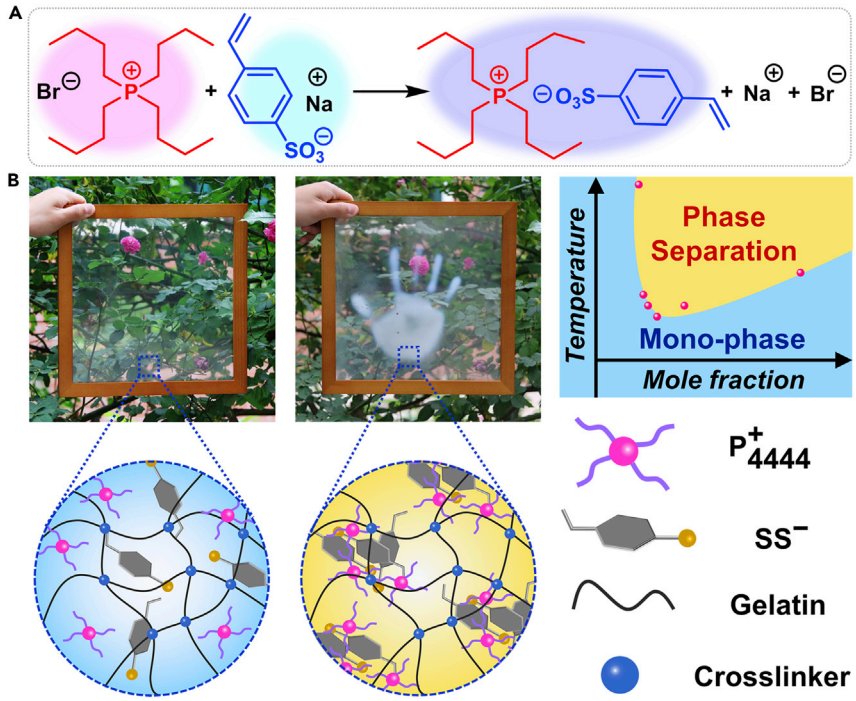

Figure 1. General view of the LCST behavior in HCIS

(A) Synthetic route of the preparation of $[P_{4444}][SS]$ resulting from ionic exchange

(B) Optical images to demonstrate the LCST behavior of HCIS. The HCIS is highly transparent under ambient temperature while it becomes turbid in the region where a human hand touches. The phase diagram depicts the critical temperature of $[P_{4444}][SS]$ in H_2O with different ratios. The mole fraction between $[P_{4444}][SS]$ and H_2O is set as 1:300, 1:200, 1:150, 1:100, 1:50, and 1:15, respectively, from left to right, and their LCSTs are 44°C, 26°C, 22°C, 20°C, 22°C, and 28°C, respectively.

the concentration of HCl from 0.1 mol•L^{-1} to 1.0 mol•L^{-1} under a given temperature of 44°C, the solution becomes increasingly transparent (Figure 2B), yet the UV-vis spectra indicate the LCST owns a downward trend (Figures 2C and S2A). With increasing the concentration of NaCl from 0 to 1.7 mol•L^{-1} in the $[P_{4444}][SS]$ aqueous solution, the system experienced a transition from transparent to turbid at the temperature of 44°C (Figure 2D). According to the transmittance change as a function of NaCl concentration, the LCST goes up first and then drops (Figures 2E and S2B). Similar phase behaviors responsible for HCl and NaCl addition were also observed under other temperatures (Figures S3 and S4).

Mechanism of the LCST variation with the application of HCl or NaCl

The temperature-dependent molecular interaction between $[P_{4444}][SS]$ and water was investigated by ^1H NMR spectrometer aiming to explain the LCST behaviors in the presence of HCl or NaCl. As illustrated in Figure 3A, the proton signals assigned to $[P_{4444}][SS]$ first shift to upfield with a chemical shift change of 0.062 ppm after the addition of 0.2 mol•L^{-1} HCl. With increasing the temperature from 25°C to 55°C, the proton signals shift to downfield gradually with an interval of 0.095 ppm every 10°C. The thermally induced downfield shift is attributed to the breaking of hydrogen bonds between $[P_{4444}][SS]$ and water (Tsai and Lin, 2019). To be specific, the hydrogen bonding interaction exists between the O atom of the $[SS]^-$ anion and the H atom of the H_2O. The weakened hydrogen bond at higher temperature strengthens the shielding effect on the H atom of water molecules, which should lead to the upfield shift of proton signals of water. Namely, if the D_2O signal at 4.60 ppm is set as the reference, the proton signals of $[P_{4444}][SS]$ relative to D_2O signal show downfield shift upon increasing the temperature. As control experiments, two aprotic solvents including chloroform-d and dimethyl sulfoxide-d6 were used to replace D_2O for the temperature-dependent ^1H NMR studies (Figures S5 and S6). Without forming hydrogen bonds between $[P_{4444}][SS]$ and solvents, scarce changes of chemical shift were observed in both cases.

According to NMR investigations, the influence of HCl to LCST behaviors is ascribed to the solvation process. Once $[P_{4444}][SS]$ is dissolved in H_2O, the hydration occurs particularly on $[SS]^-$ anions in light of the

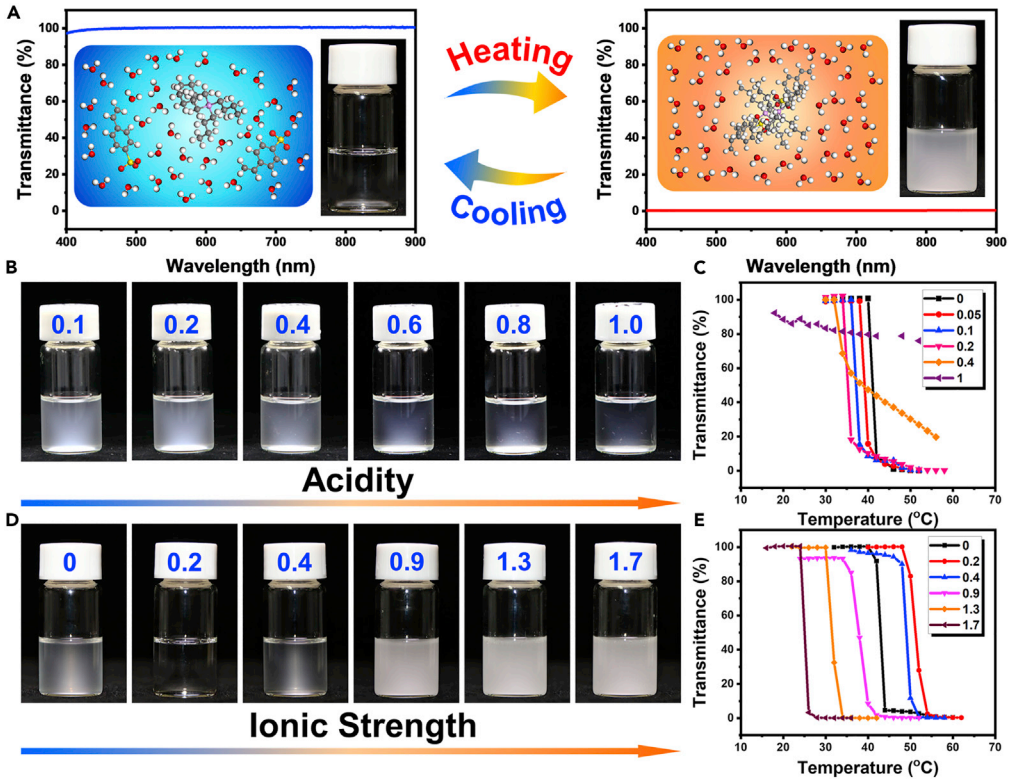

Figure 2. Adjustable critical temperature of $[P_{4444}][SS]$ in H_2O

(A) The investigation of LCST behaviors by UV-Vis spectrometer. Upon heating, the transmittance is reduced from 99.0% to 0.4%, which is totally reversible. Insets show the molecular states of $[P_{4444}][SS]$ along with LCST behavior.

(B) Optical images of the LCST behavior of $[P_{4444}][SS]$ aqueous solution in the presence of different concentrations of HCl. The temperature is fixed at 44°C.

(C) Transmittance of the $[P_{4444}][SS]$ aqueous solution as a function of temperature upon addition of HCl with different concentrations.

(D) Optical images of the LCST behavior of $[P_{4444}][SS]$ aqueous solution in the presence of different concentrations of NaCl. The temperature is fixed at 44°C.

(E)Transmittance of the $[P_{4444}][SS]$ aqueous solution as a function of temperature upon addition of NaCl with different concentrations.

hydrogen bonding interaction. $[P_{4444}]^+$ is hardly able to be hydrated by water owing to its hydrophobic alkyl chain. That is, $[P_{4444}]^+$ is dissolved in the aqueous solution mainly based on the coulomb interaction with the counterions of $[SS]^-$. Once HCl is added into the system, water molecules prefer to interact with protons to form H_3O^+ on account of their higher binding energy. Therefore, $[SS]^-$ anions are gradually dehydrated and salted out together with $[P_{4444}]^+$ from the water medium. In the meanwhile, H_3O^+ ions compete with water molecules to form new hydrogen bonds with $[SS]^-$. However, under low HCl concentration, the limited number of this new kind of hydrogen bonds is unable to contend against the phase separation. We define this state as pseudo salt out. Further increasing the concentration of HCl, growing numbers of hydrogen bonds are predicted to exist between H_3O^+ and $[SS]^-$, leading to the formation of micellar aggregates in which hydrophobic $[P_{4444}]^+$ cations stay in the core of micelles. It is proposed that the micelles are positively charged on their surfaces and repulsive from each other. Further increasing concentration of HCl would generate more hydrogen bonds on the micelle surfaces and also reinforce the repulsion between micelles (Figure 3B). Consequently, the droplets become smaller and can be well dispersed in the system (Li et al., 2020). The solution accordingly becomes more transparent under macroscopic observation, which is fully agreed with the microscope images in Figure S7.

The addition of NaCl in $[P_{4444}][SS]$ aqueous solution results in the downfield shift of proton signal, suggesting the hydrogen bonding interaction between $[SS]^-$ and water may be corrupted by NaCl (Figures 3C and S8). Further increasing the temperature from 25°C to 55°C, a similar shift was observed owing to the

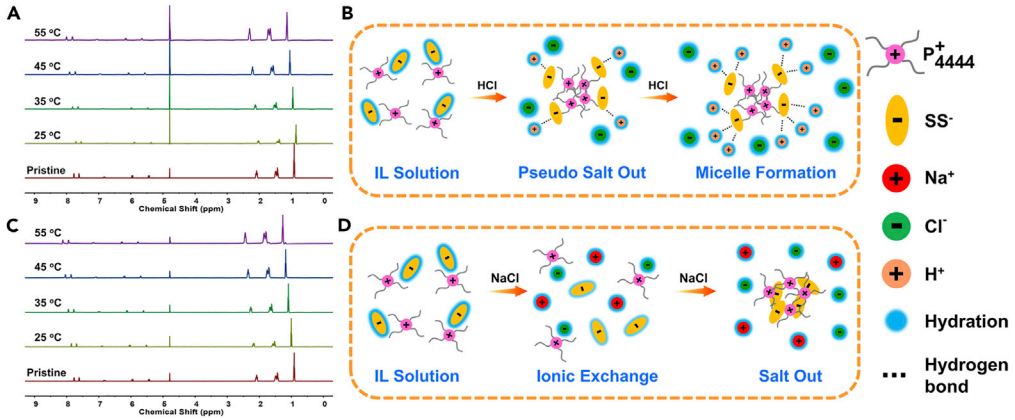

Figure 3. Mechanisms of the LCST variation upon adding HCl and NaCl

(A) Temperature-dependent ^{1}H NMR spectra of $[P_{4444}][SS]$ solution in D_2O with addition of 0.2 mol·L^{-1} HCl. The temperature ranges from 25°C to 55°C with an interval of 10°C.

(B) Schematic illustration of the mechanism of the HCl influence on LCST behaviors.

(C) Temperature-dependent ^{1}H NMR of $[P_{4444}][SS]$ solution in D_2O with addition of 0.9 mol·L^{-1} NaCl. The temperature ranges from 25°C to 55°C with an interval of 10°C.

(D) Schematic illustration of the mechanism of the NaCl influence on LCST behaviors.

gradual destruction of hydrogen bond at higher temperature. However, this hydrogen-bond-dominated theory fails to explain the increase of LCST under low NaCl concentration. Hence, we assume that the LCST of this system is dominated by two processes, including the ionic exchange and salt-out effect (Men et al., 2012; Wang et al., 2010). In principle, when NaCl is added into the solution, Na^+ and Cl^- are both hydrated by water molecules. Under low NaCl concentration, though the hydration of $[SS]^-$ is slightly weakened, the ionic exchange surpasses this weakened hydration and improves the solubility of the system. Concretely, $[P_{4444}]^+$ cation prefers to interact with Cl^- compared to $[SS]^-$ owing to the stronger Coulomb interaction. The more hydrophilic nature of Cl^- can better stabilize $[P_{4444}]^+$ in aqueous solution than $[SS]^-$. Likewise, $[SS]^-$ can be stabilized by Na^+ rather than $[P_{4444}]^+$. As a result, the better solubility of $[P_{4444}][SS]$ induced by ionic exchange corresponds to a higher LCST. However, continuous addition of NaCl will further weaken the hydration of $[SS]^-$ until the ionic exchange effect fails to sustain the stability of $[P_{4444}]^+$ and $[SS]^-$, resulting in the salt-out effect at high NaCl concentration, and, therefore, the LCST is decreased (Figure 3D). The different influences on LCST behavior between HCl and NaCl originate from their affinity with H_2O. Owing to the relative higher binding energy of H^+ with H_2O, the contribution led by ionic exchange in the case of HCl addition can be ignored and the pseudo salt-out effect is predominant.

Intuitive demonstration of the LCST adjustment with NaCl

$[P_{4444}][SS]$ was confined within a hydrogel to realize freestanding performance while retaining its LCST behavior. It is worth noting that the adjustment of LCST can be also accomplished in the gelatin-based hydrogel network. NaCl is superior to HCl for adjusting LCST within HCIS because the latter may cause the hydrolysis of gel network. As illustrated in Figure 4A, $[P_{4444}][SS]$ is dispersed homogeneously in the hydrogel. Once NaCl is added into the system, the LCST of the HCIS is changed which relies on the NaCl concentration. To intuitively demonstrate the effect of NaCl, a brush pen soaked with 3.0 mol·L^{-1} NaCl solution was used to write NaCl patterns on the hydrogel (Figure 4B). As shown in Figure 4C, the hydrogel is transparent and clear before the brush pen-writing NaCl at a temperature of 35°C. After written with NaCl solution, a picture of a panda eating bamboo shows up. More than that, the hydrogel could be written with different concentrations of NaCl solutions to reach a temperature-resolved imaging display. As exemplified in Figure 4D, when the temperature rises to 27°C, the stars written by 5.0 mol·L^{-1} NaCl solution are firstly emerged. And when the temperature further rises to 45°C, a rabbit written by 3.0 mol·L^{-1} NaCl solution shows up in the grass.

Thermal field visualization with HCIS

With the unique advantage of adjustable LCST, the HCIS was applied to visualize the spatial distribution of thermal field. As a representative demonstration, a 25.0 × 25.0 × 25.0 mm^3 cube with a quartz tube

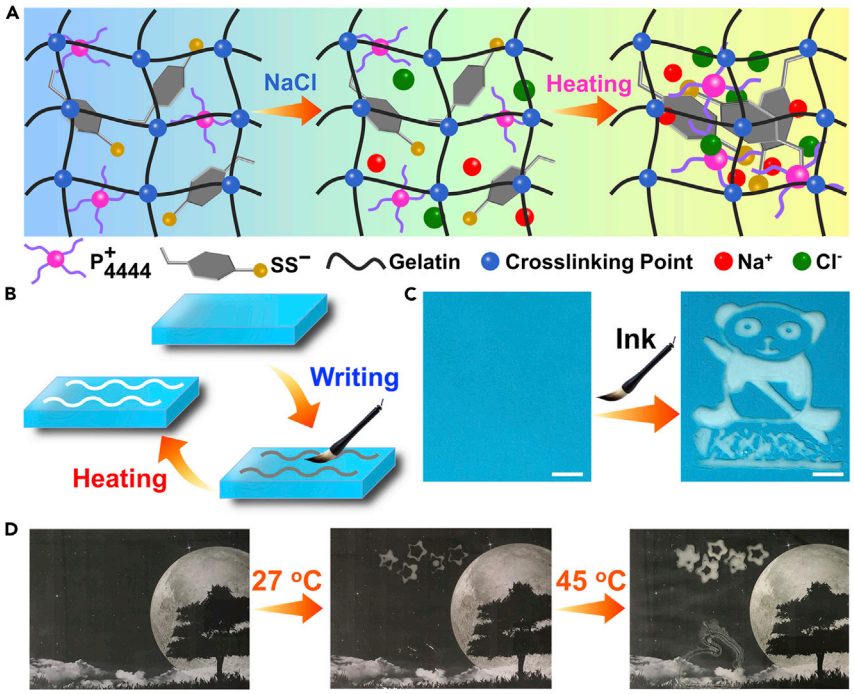

Figure 4. The adjustment of LCST within HCIS by means of NaCl addition

(A) Schematic illustration of the LCST behaviors within HCIS as a result of phase separation from the molecular view.

(B) Schematic illustration of the brush pen-writing method to build NaCl patterns on HCIS.

(C) Optical images of the NaCl-patterned HCIS to present thermal imaging of a panda sitting on grassland and eating bamboo. The HCIS film was first heated to 35°C and then patterned with 3.0 mol·L^{-1} NaCl solution. The scale bar is 2.0 cm.

(D) Temperature-resolved thermal imaging of NaCl-patterned HCIS. The HCIS was patterned stars with 5.0 mol·L^{-1} NaCl solution and a rabbit with 3.0 mol·L^{-1} NaCl solution in advance. As the temperature increased to 27°C, the stars appeared first owing to the lower LCST caused by higher NaCl concentration. Subsequently, as the temperature increased to 45°C, the rabbit was emerged on the grassland and the stars became clearer.

across its center was fabricated to visualize thermal distribution in a 3D pattern. Filling the tube with 25°C water rarely caused turbidity change from the side and front view because the temperature was below the LCST. When the water temperature increased to 40°C (>LCST), a turbid cylinder with the diameter of 5.4 mm was observed due to the propagation of thermal field (Figure 5B). Further increasing the temperature to 50°C (Figure 5C) and 60°C (Figure 5D), the diameter of the cylinder increased to 8.7 mm and 10.7 mm, respectively. In addition, the 3D imaging of thermal field distribution is totally reversible. Pumping hot and cold water alternatively could generate and erase thermal field images repeatedly (Video S1). The thermal field simulation is fully consistent with the experimental observations under different temperatures both in trend and size (Figures 5 and S9B). The convective heat transfer coefficient under different temperatures could be calculated according to the thermal field simulation, and more details were accessible in the supplemental information. These results have passed the grid independence test (Figure S9A). It is worth noting that the thermal field distribution in the chamber could not be monitored with an infrared imager at all because of the reflection caused by the wall and the limited penetration depth of infrared light.

A 5 × 5 tube array sealed in the HCIS was established to validate whether the HCIS was capable of visualizing sophisticated thermal distribution in daily life. In this array, the thermal field could be programmed to form different thermal images spatially with the application of the water with different temperatures at different sites. As illustrated in Figures 5I and 5J, the electron cloud of *p* orbit and a letter "Y" were demonstrated by applying water with 0°C and 60°C. As stated above, different temperatures of the thermal source will result in different radiation diameters in HCIS. Therefore, a *d* orbit-like image was designed (Figure 5K) with 50°C water going through left and right tubes, while 60°C water going through up and down tubes. Water at 0°C went through the middle, upleft, upright, lower left, and lower right tubes to cut off the

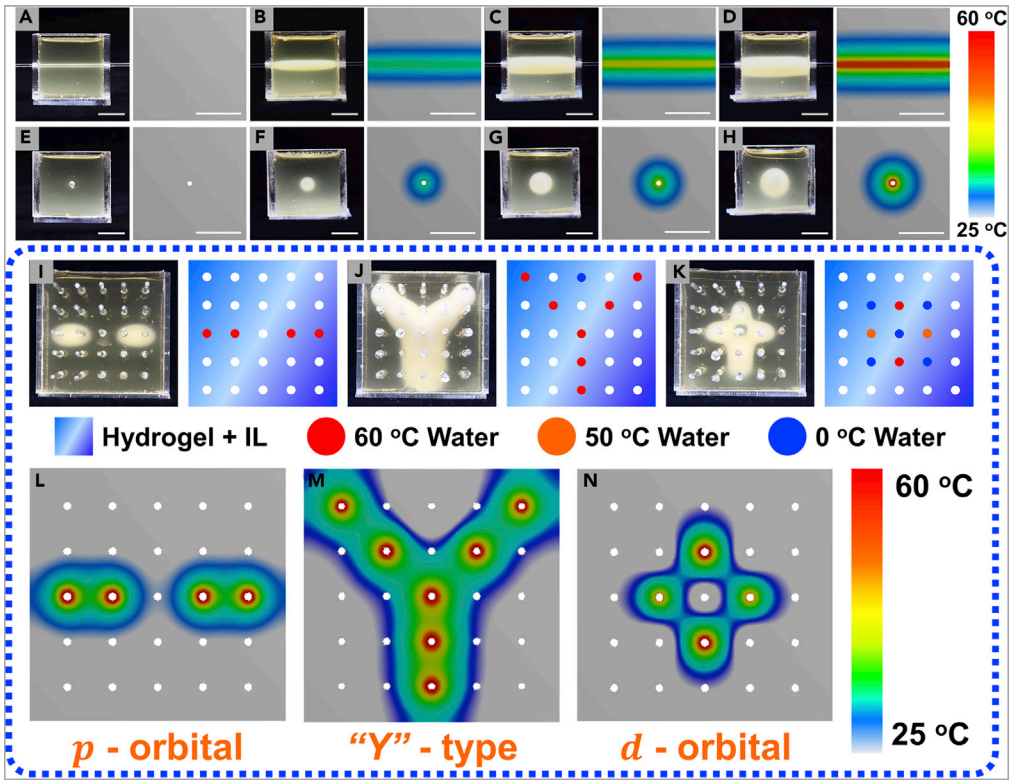

Figure 5. Visualizing thermal distribution with HCIS

(A–D) Side views of spatial thermal distribution together with their simulation results. The temperatures in the quartz tubes were set as 25°C, 40°C, 50°C, and 60°C, respectively.

(E–H) Front views of spatial thermal distribution together with their simulation results. The temperatures in the quartz tubes were set as 25°C, 40°C, 50°C, and 60°C, respectively. The radiation diameters of the thermal fields were 0, 5.4 mm, 8.7 mm, and 10.7 mm, respectively. The scale bars are 2.0 cm.

(I–K) Visualizing sophisticated spatial thermal distribution in a 5 × 5 array.

thermal field propagation. Computational simulations were also used to depict the thermal field superposition state (Figures 5L–5N). Notably, the simulation results correspond well with experimental results. Small deviations between experimental results and simulation results could be observed on the upper part of "Y" and the *d* orbit. This is a perturbation caused by an evanescent decay of thermal energy on the top of the hydrogel.

Fire warning system with the application of HCIS

To reveal the importance of visualizing thermal field, the HCIS was successfully extended to a fire warning system. Nowadays, the fire hazard has become one of the most threatening accidents. It is shocking that over 380,000 fire disasters happened in China in 2018 and thousands of people were killed, letting alone the billions of property damage. Among all the fire disasters, residential fires caused the highest ratio of casualties up to 57.5%. Most residential fires originate from electrical failure caused overheating, such as short circuit, breakdown, aging, and so on (Figure 6A). This is also one of the possible reasons for the tragedy of Notre-Dame de Paris. If the thermal energy could have been observed real-timely, quantities of lives and property would be saved in time. Here, we managed to cover HCIS on the surface of the electrical wire, and a transparent sealing shell was designed to prevent the evaporation of H_2O from the hydrogel matrix (Figure 6B). The fire warning system is highly transparent under secure condition, and electric wires can be clearly seen. However, when the electrical failure occurs, the electric wires start to heat up and higher turbidity appears at the thermal field superposition site (the middle of "R"). If the "caution" state is ignored, the turbid area will be enlarged along the electric wire direction owing to the continuous heating to further attract people's attention. The phase separation of ionic liquid indicates that the electric wires are overheated and fire hazard would occur sooner or later.

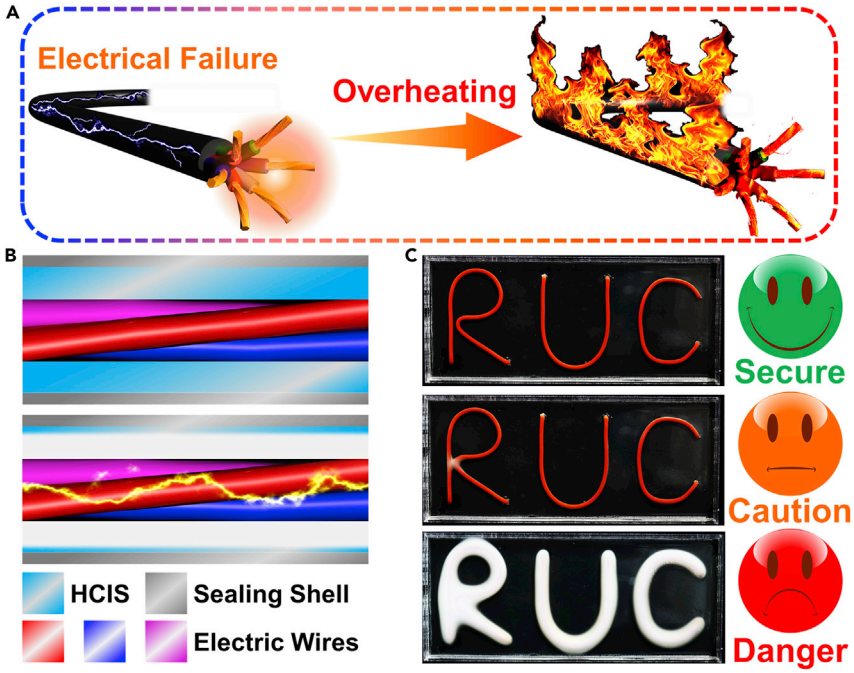

Figure 6. Thermal imaging for a fire warning system

(A) Schematic illustration of fire hazard induced by electrical failures.

(B) Schematic illustration of a fire warning system. Under normal condition, the HCIS is transparent and the electric wires can be seen. When electrical failure occurs, the HCIS becomes turbid and the electric wires are covered by the hydrogel with phase separation.

(C) Model experiments to demonstrate the availability of fire warning system. Three conditions are demonstrated: secure (none overheated), caution (local overheated), and danger (Overheated).

DISCUSSION

In summary, a hydrogel confined ionic system has been formulated to visualize the thermal distributions that are difficult to be monitored by thermal imagers. The LCST behavior of the ionic liquid ($[P_{4444}][SS]$), which is relevant to the hydrogen bond between $[SS]^-$ and H_2O, leads to the phase separation above the critical temperature and turns the hydrogel from transparent to turbid. The critical temperature of the system is adjustable with the different concentrations of HCl and NaCl. Further research revealed that the adjustment capacity originates from the pseudo salt-out effect at low HCl concentrations and micelle formation at high HCl concentrations. For NaCl, the adjustment capacity is the result of ionic exchange at low concentrations and salt-out effect at high NaCl concentrations. Unlike thermal-responsive polymer system, e.g., poly (N-isopropylacrylamide), in which LCST behavior results from phase separation between polymer and solvent, the strategy of HCIS does not involve the problems of water loss and volume shrinkage.

The HCIS was successfully exploited to visualize thermal distribution in an easy way. The tunable LCST enhanced its universality for many scenarios of production and life. The economical and eco-friendly features of hydrogel greatly promote the practical significance of the HCIS. Moreover, the HCIS can work as a fire warning system to lower the threat induced by electrical failure. This research provides a practical way to visualize thermal distribution directly based on simple yet efficient materials. The HCIS may render great convenience for us to better regulate thermal energy in our daily life and industrial production.

Limitations of the study

Aside from these breakthroughs, we admit some imperfections exist in the HCIS. First of all, the most significant disadvantage is the salt diffusion during local LCST regulation. The diffusion of NaCl will make the pattern unstable and lower the resolution of thermal imaging. What's more, the HCIS has a weak ability to distinguish temperature. To solve these problems, gradient LCST in the same material is essentially needed, which will be realized in our next work.

Resource availability

Lead contact

Further requests for resources and materials should be directed to the lead contact, Yapei Wang (yapeiwang@ruc.edu.cn).

Material availability

This study did not use or generate any reagents.

Data and code availability

This study did not generate large-scale data sets or novel unique analysis code. All data are described in the main text and all analysis methods in the Supplemental information.

METHODS

All methods can be found in the accompanying Transparent Methods supplemental file.

SUPPLEMENTAL INFORMATION

Supplemental information can be found online at https://doi.org/10.1016/j.isci.2021.102085.

ACKNOWLEDGMENTS

This work was financially supported by the National Natural Science Foundation of China (21825503, 21674127).

AUTHOR CONTRIBUTIONS

Conceptualization, Y.W., Y.H., and Q.G.; Methodology Q.G., B.F., and Y.H.; Software, S.L.; Validation, Q.G., B.F., Y.H., S.L., Y.M., and Y.W.; Formal Analysis, Q.G., B.F., and S.L.; Investigation, Q.G. and B.F.; Writing-Original Draft, Q.G., Writing-Review & Editing, B.F. and Y.W.; Visualization, Q.G., B.G., and Y.H.; Supervision, Y.W.; Funding Acquisition, Y.W.

DECLARATION OF INTERESTS

The authors declare no competing interests.

Received: November 24, 2020
Revised: January 7, 2021
Accepted: January 15, 2021
Published: February 19, 2021

REFERENCES

Alf, M.E., Hatton, T.A., and Gleason, K.K. (2011). Insights into thin, thermally responsive polymer layers through quartz crystal microbalance with dissipation. Langmuir *27*, 10691–10698.

Cao, Y., Dou, J.-H., Zhao, N., Zhang, S., Zheng, Y.-Q., Zhang, J.-P., Wang, J.-Y., Pei, J., and Wang, Y. (2017). Highly efficient NIR-II photothermal conversion based on an organic conjugated polymer. Chem. Mater. *29*, 718–725.

Chen, G., Yu, Y., Wu, X., Wang, G., Ren, J., and Zhao, Y. (2018). Bioinspired multifunctional hybrid hydrogel promotes wound healing. Adv. Funct. Mater. *28*, 1801386.

Choi, E., and Yethiraj, A. (2015). Entropic Mechanism for the lower critical solution temperature of poly(ethylene oxide) in a room temperature ionic liquid. ACS Macro Lett. *4*, 799–803.

Fukumoto, K., and Ohno, H. (2007). LCST-type phase changes of a mixture of water and ionic liquids derived from amino acids. Angew. Chem. Int. Ed. Engl. *46*, 1852–1855.

Gao, J., Guo, J., Nie, F., Ji, H., and Liu, S. (2017). LCST-type phase behavior of aqueous biphasic systems composed of phosphonium-based ionic liquids and potassium phosphate. J. Chem. Eng. Data *62*, 1335–1340.

Gao, N., He, Y., Tao, X., Xu, X.-Q., and Wang, Y. (2019). Crystal-confined freestanding ionic liquids for reconfigurable and repairable electronics. Nat. Commun. *10*, 547.

Gui, Q., He, Y., Gao, N., Tao, X., and Wang, Y. (2017). A skin-inspired integrated sensor for synchronous monitoring of multiparameter signals. Adv. Funct. Mater. *27*, 1702050.

He, Y., Liao, S., Jia, H., Cao, Y., Wang, Z., and Wang, Y. (2015). A self-healing electronic sensor based on thermal-sensitive fluids. Adv. Mater. *27*, 4622–4627.

He, Y., Gui, Q., Wang, Y., Wang, Z., Liao, S., and Wang, Y. (2018). A polypyrrole elastomer based on confined polymerization in a host polymer network for highly stretchable temperature and strain sensors. Small *14*, 1800394.

Kohno, Y., Deguchi, Y., and Ohno, H. (2012). Ionic liquid-derived charged polymers to show highly thermoresponsive LCST-type transition with water at desired temperatures. Chem. Commun. *48*, 11883–11885.

Li, J.-J., Zhou, Y.-N., Luo, Z.-H., and Zhu, S. (2019a). A polyelectrolyte-containing copolymer with a gas-switchable lower critical solution temperature-type phase transition. Polym. Chem. *10*, 260–266.

Li, X.-H., Liu, C., Feng, S.-P., and Fang, N.X. (2019b). Broadband light management with

thermochromic hydrogel microparticles for smart windows. Joule *3*, 290–302.

Li, C., Iscen, A., Palmer, L.C., Schatz, G.C., and Stupp, S.I. (2020). Light-driven expansion of spiropyran hydrogels. J. Am. Chem. Soc. *142*, 8447–8453.

Lu, B., Yuk, H., Lin, S., Jian, N., Qu, K., Xu, J., and Zhao, X. (2019). Pure PEDOT:PSS hydrogels. Nat. Commun. *10*, 1043.

Lyu, S., He, Y., Yao, Y., Zhang, M., and Wang, Y. (2019). Photothermal clothing for thermally preserving pipeline transportation of crude oil. Adv. Funct. Mater. *29*, 1900703.

Matsumoto, K., and Endo, T. (2008). Confinement of ionic liquid by networked polymers based on multifunctional epoxy resins. Macromolecules *41*, 6981–6986.

Men, Y., Li, X.-H., Antonietti, M., and Yuan, J. (2012). Poly(tetrabutylphosphonium 4-styrenesulfonate): a poly(ionic liquid) stabilizer for graphene being multi-responsive. Polym. Chem. *3*, 871–873.

Men, Y., Schlaad, H., and Yuan, J. (2013). Cationic poly(ionic liquid) with tunable lower critical solution temperature-type phase transition. ACS Macro Lett. *2*, 456–459.

Ota, H., Chen, K., Lin, Y., Kiriya, D., Shiraki, H., Yu, Z., Ha, T.-J., and Javey, A. (2014). Highly deformable liquid-state heterojunction sensors. Nat. Commun. *5*, 5032.

Qiao, Y., Ma, W., Theyssen, N., Chen, C., and Hou, Z. (2017). Temperature-responsive ionic liquids: fundamental behaviors and catalytic applications. Chem. Rev. *117*, 6881–6928.

Shchukina, E.M., Graham, M., Zheng, Z., and Shchukin, D.G. (2018). Nanoencapsulation of phase change materials for advanced thermal energy storage systems. Chem. Soc. Rev. *47*, 4156–4175.

Tao, X., Jia, H., He, Y., Liao, S., and Wang, Y. (2017). Ultrafast paper thermometers based on a green sensing ink. ACS Sens. *2*, 449–454.

Tsai, Y.-R., and Lin, S.-T. (2019). Prediction and reasoning for the occurrence of lower critical solution temperature in aqueous solution of ionic liquids. Ind. Eng. Chem. Res. *58*, 10064–10072.

Ueki, T., Nakamura, Y., Yamaguchi, A., Niitsuma, K., Lodge, T.P., and Watanabe, M. (2011). UCST phase transition of azobenzene-containing random copolymer in an ionic liquid. Macromolecules *44*, 6908–6914.

Wang, J. (2020). Innovating ionic liquids as repairable electronics for liquid robots. Green. Energy Environ. *5*, 122–123.

Wang, H., Feng, Q., Wang, J., and Zhang, H. (2010). Salt effect on the aggregation behavior of 1-decyl-3-methylimidazolium bromide in aqueous solutions. J. Phys. Chem. B *114*, 1380–1387.

Wang, Y., Gong, S., Wang, S.J., Simon, G.P., and Cheng, W. (2016). Volume-invariant ionic liquid microbands as highly durable wearable biomedical sensors. Mater. Horiz. *3*, 208–213.

Wang, C., Hua, L., Yan, H., Li, B., Tu, Y., and Wang, R. (2020). A thermal management strategy for electronic devices based on moisture sorption-desorption processes. Joule *4*, 425–447.

Yang, Q., Zhang, Z., Sun, X.-G., Hu, Y.-S., Xing, H., and Dai, S. (2018a). Ionic liquids and derived materials for lithium and sodium batteries. Chem. Soc. Rev. *47*, 2020–2064.

Yang, Y., Wang, X., Yang, F., Wang, L., and Wu, D. (2018b). Highly elastic and ultratough hybrid ionic–covalent hydrogels with tunable structures and mechanics. Adv. Mater. *30*, 1707071.

Yu, C., Guo, H., Cui, K., Li, X., Ye, Y.N., Kurokawa, Y., and Gong, J.P. (2020). Hydrogels as dynamic memory with forgetting ability. Proc. Natl. Acad. Sci. U S A *117*, 18962–18968.

Zhang, P., Sun, F., Tsao, C., Liu, S., Jain, P., Sinclair, A., Hung, H.-C., Bai, T., Wu, K., and Jiang, S. (2015). Zwitterionic gel encapsulation promotes protein stability, enhances pharmacokinetics, and reduces immunogenicity. Proc. Natl. Acad. Sci. U S A *112*, 12046–12051.

Zhao, D., Zhu, Y., Cheng, W., Xu, G., Wang, Q., Liu, S., Li, J., Chen, C., Yu, H., and Hu, L. (2020a). A dynamic gel with reversible and tunable topological networks and performances. Matter *2*, 390–403.

Zhao, Y., Zhang, B., Yao, B., Qiu, Y., Peng, Z., Zhang, Y., Alsaid, Y., Frenkel, I., Youssef, K., Pei, Q., and He, X. (2020b). Hierarchically structured stretchable conductive hydrogels for high-performance wearable strain sensors and supercapacitors. Matter *3*, 1196–1210.

Zhou, L., Tan, Y., Ji, D., Zhu, B., Zhang, P., Xu, J., Gan, Q., Yu, Z., and Zhu, J. (2016). Self-assembly of highly efficient, broadband plasmonic absorbers for solar steam generation. Sci. Adv. *2*, e1501227.

Zhou, Y., Wan, C., Yang, Y., Yang, H., Wang, S., Dai, Z., Ji, K., Jiang, H., Chen, X., and Long, Y. (2019). Highly stretchable, elastic, and ionic conductive hydrogel for artificial soft electronics. Adv. Funct. Mater. *29*, 1806220.

Zhou, Y., Wang, S., Peng, J., Tan, Y., Li, C., Boey, F.Y.C., and Long, Y. (2020). Liquid thermo-responsive smart window derived from hydrogel. Joule *4*, 1–17.

Ziolkowski, B., and Diamond, D. (2013). Thermoresponsive poly(ionic liquid) hydrogels. Chem. Commun. *49*, 10308–10310.

iScience, Volume *24*

Supplemental Information

Visualizing thermal distribution through hydrogel confined ionic system

Qinyuan Gui, Bin Fu, Yonglin He, Shanzhi Lyu, Yingchao Ma, and Yapei Wang

1. Supplemental Figures

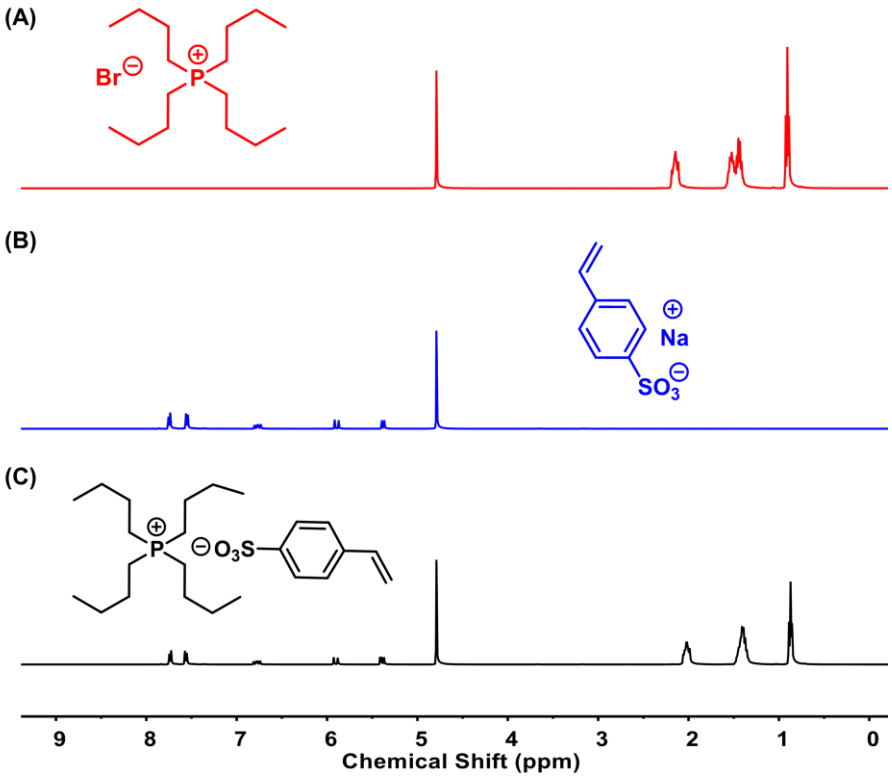

Fig. S1. ^{1}H NMR spectra of the raw materials and product. ^{1}H NMR of [P_{4444}]Br (A), Na[SS] (B) and [P_{4444}][SS] (C). Related to Fig. 1.

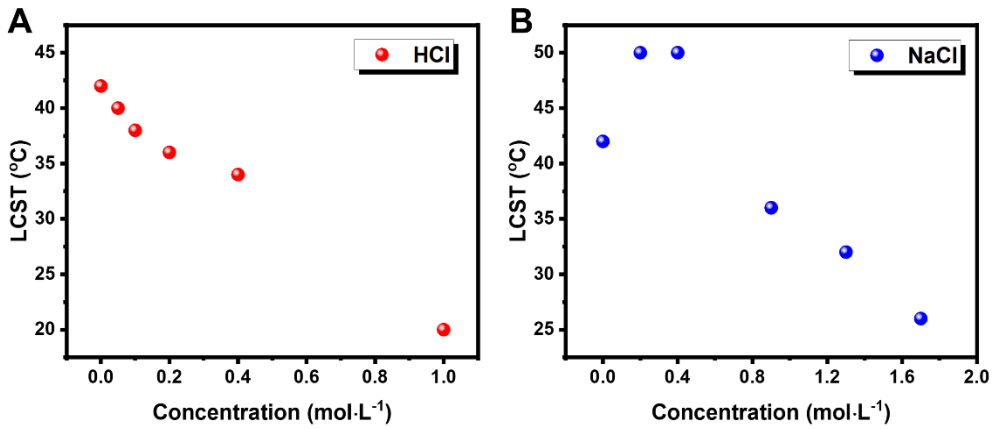

Fig. S2. LCST of IL-H2O binary system as a function of regulator concentration. **(A)** The concentrations of HCl were 0, 0.05, 0.1, 0.2, 0.4 and 1 mol·L^{-1} from left to right, respectively. **(B)** The concentrations of NaCl were 0, 0.2, 0.4, 0.9, 1.3 and 1.7 mol·L^{-1} from left to right, respectively. Related to Fig. 2.

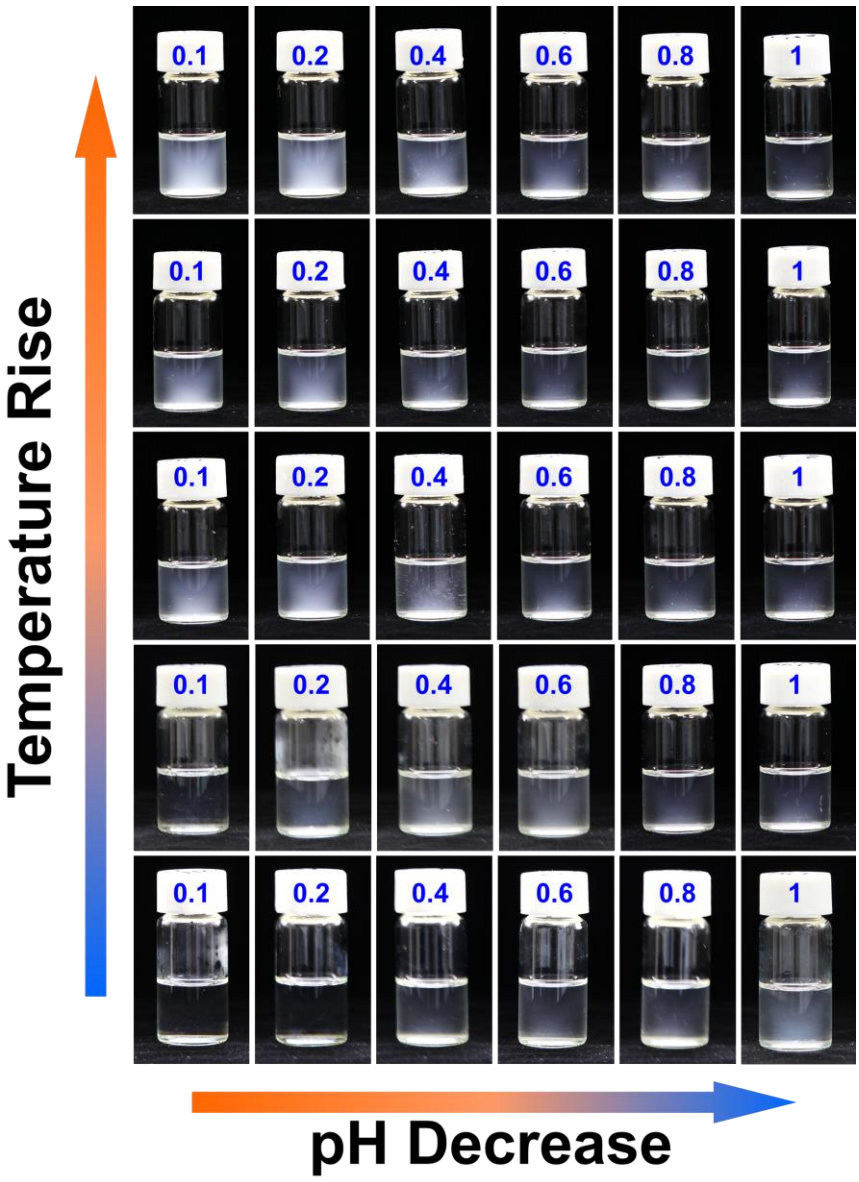

Fig. S3. Optical images of the turbidity of [P_{4444}][SS] aqueous solution applied with various concentrations of HCl under different temperatures. The concentrations of HCl were 0.1, 0.2, 0.4, 0.6, 0.8 and 1 mol·L^{-1} from left to right, respectively. The temperature increased from 36 to 44 ^{o}C with an interval of 2 ^{o}C. Related to Fig. 2.

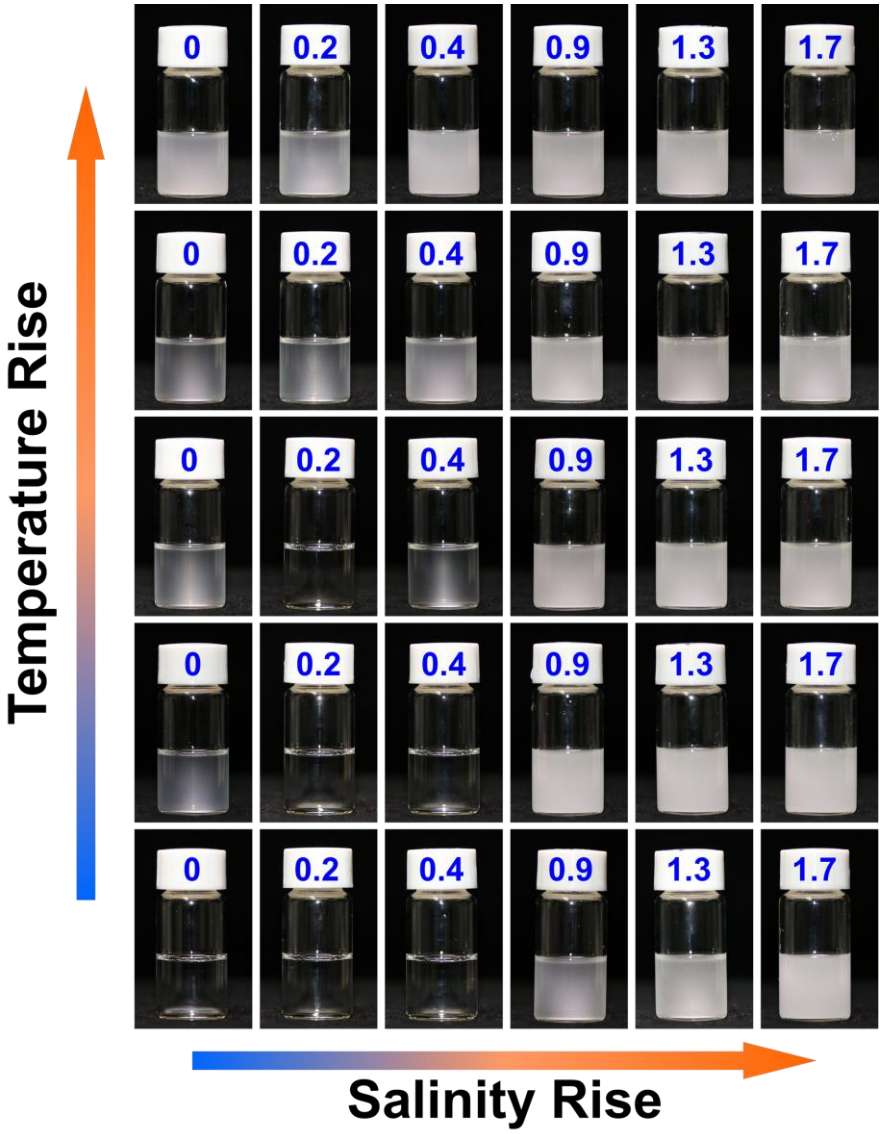

Fig. S4. Optical images of the turbidity of [P_{4444}][SS] aqueous solution applied with various concentrations of NaCl under different temperatures. The concentrations of NaCl were 0, 0.2, 0.4, 0.9, 1.3 and 1.7 mol·L^{-1} from left to right, respectively. The **temperatures** were 35, 42, 44, 46, 48 ºC from the bottom to the top, respectively. Related to Fig. 2.

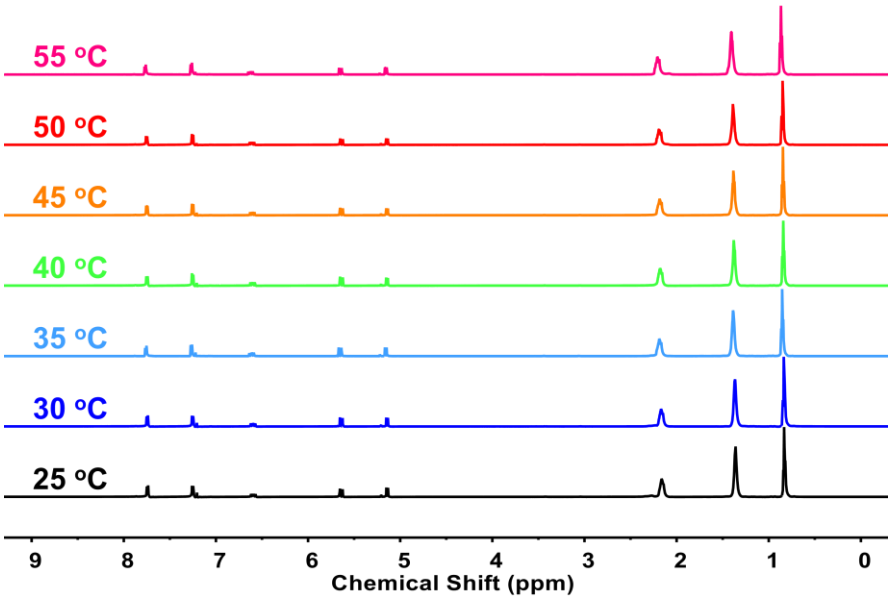

Fig. S5. Temperature-dependent ^{1}H NMR spectra of [P_{4444}][SS] in $CDCl_3$. The temperature increased from 25 °C to 55 °C with an interval of 5 °C. Chemical shifts were not observed in this aprotic solvent. Related to Fig. 3.

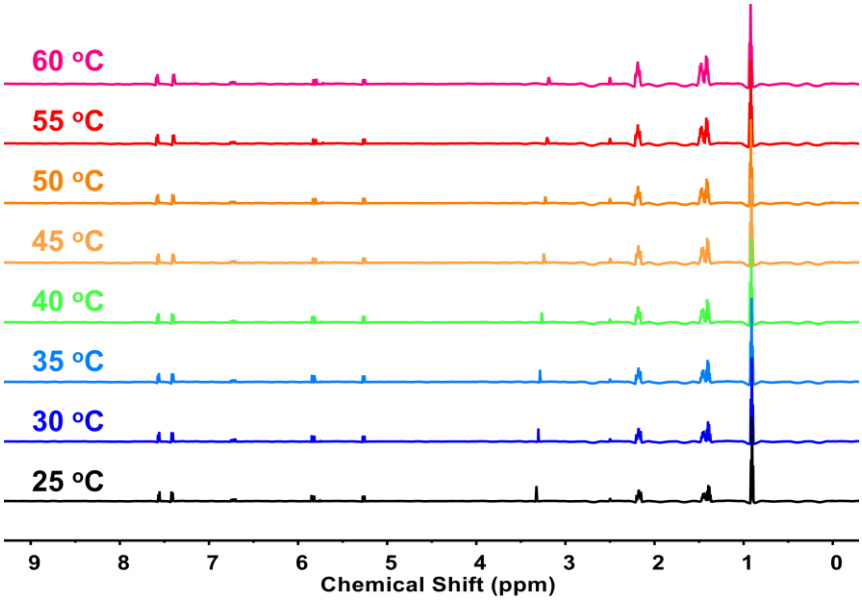

Fig. S6. Temperature-dependent ^{1}H NMR spectra of [P_{4444}][SS] in DMSO-d6. The temperature increased from 25 °C to 60 °C with an interval of 5 °C. The proton signal at 3.325 ppm corresponding to the remanent H_2O under 25 °C moved gradually to 3.188 ppm upon increasing the temperature to 60 °C. Beyond that, each peak retained its own position as the temperature increased. Related to Fig. 3.

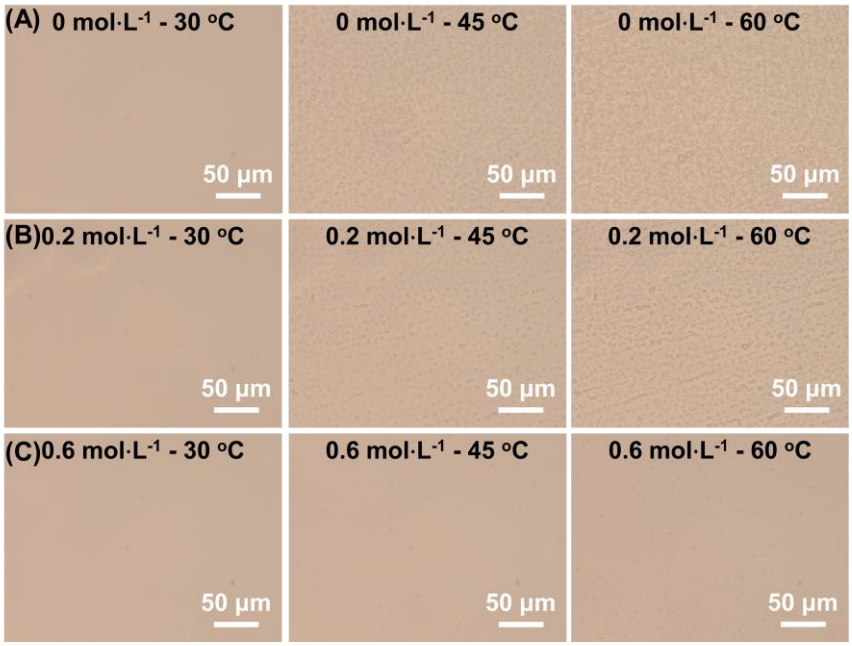

Fig. S7. Microscopic images of precipitated [P_{4444}][SS] droplets under different concentrations of HCl. (A) Pure [P_{4444}][SS] solution without the addition of HCl started phase separation under 45 °C and the droplet size continued growing with the increasing temperature. **(B)** In the case of the addition with 0.2 mol·L^{-1} HCl, the precipitated droplets were smaller than pure [P_{4444}][SS] solution under 45 °C and 60 °C. **(C)** The droplets became even smaller after the addition of 0.6 mol·L^{-1} HCl. For all the samples, the molar ratios between [P_{4444}][SS] were set as 1:300. Related to Fig. 3.

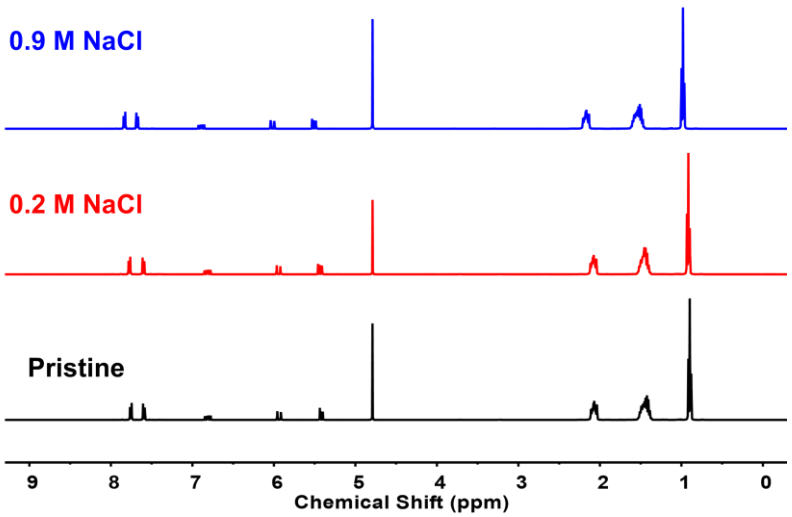

Fig. S8. ^{1}H NMR spectra of [P_{4444}][SS] in D_2O with the addition of different concentrations of NaCl. Keeping the temperature at 25 ^{o}C, the peak shifted to downfield for 0.024 ppm with the addition of 0.2 mol·L^{-1} NaCl. Further increasing the concentration of NaCl to 0.9 mol·L^{-1}, the proton signal moved downfield for 0.058 ppm. The downfield shift of the proton signal was indicative of the weakened hydration of the IL by NaCl. Related to Fig. 3.

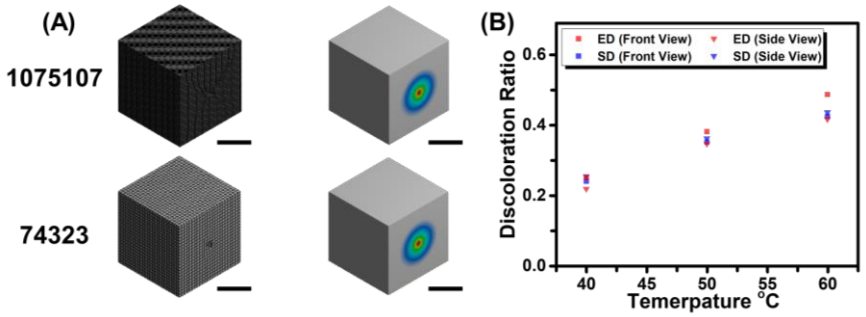

Fig. S9. The grid independence test of 3D thermal field simulation. (A) The cubic was divided into 74323 parts and 1075107 parts to perform the thermal field simulation. The consistent thermal field distribution indicated the simulation was grid-independent. The scale bar in the figure was 1.0 cm. **(B)** Comparisonbetween the radiation diameter between the experimental data (ED) and the simulated data (SD). Related to Fig. 5.

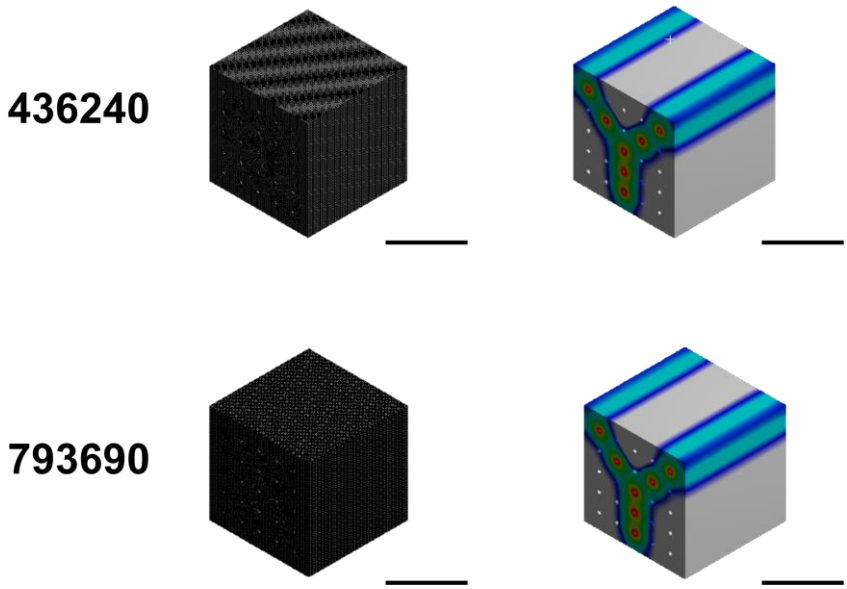

Fig. S10. The grid independence test of sophisticated thermal field simulation. The cubic was divided into 436240 parts and 793690 parts to perform the thermal field simulation. The consistent thermal field distribution indicated the simulation was grid-independent. Furthermore, the simulation results are consistent with the experimental results.The scale bar in the figure was 2.0 cm. Related to Fig. 5.

2. Supplemental Tables

Table S1. The thermal conductivity of water (λ) at different temperatures. Related to Fig. 5.

Temperature (ºC)	0	25	40	50	60
λ (W/m K)	0.551	0.609	0.635	0.648	0.659

Table S2. The Prandtl number (Pr) and Reynolds number (Re) at different temperatures. Related to Fig. 5.

Temperature (ºC)	0	25	40	50	60
Pr	13.67	6.22	4.31	3.54	2.99
Re	892	1763	2423	2871	3340

3. Description for Movie S1

Movie S1. Repeated thermal imaging and erasing with HCIS. A 25.0×25.0×25.0 mm^3 cubic was filled by HCIS with a quartz tube across its center. 50 ºC and 0 ºC water werepumped into the quartz tube alternatively. The thermal imaging caused by 50 ºC water was erased as the 0 ºC water was pumped into the quartz tube. Related to Fig. 5.

4. Transparent Methods

Materials

Tetra-n-butylphosphonium Bromide ($[P_{4444}]Br$, 99%) and sodium p-styrenesulfonate (Na[SS], 90%) were purchased from Tianjin Heowns Biochem LLC. Gelatin (~250 g Bloom) and glutaraldehyde ($C_5H_8O_2$, 50% in H_2O) were obtained from Aladdin, Shanghai, China. Dichloromethane (CH_2Cl_2, AR) was supplied by the Beijing Tong Guang Fine Chemicals Company. Sodium chloride was purchased from Energy

Chemical, China. Hydrochloric acid (A.R.) was purchased from the Huanghua Shiji Kebo Technology Development Co., Ltd.

Synthesis of [P_{4444}][SS]

[P_{4444}][SS] was synthesized through an ionic exchange reaction. Typically, 10.0 g of [P_{4444}]Br was dissolved in 50.0 mL of water, followed by the addition of 6.5 g of Na[SS]. Na[SS] was slightly excessive relative to [P_{4444}]Br to ensure the complete consumption of [P_{4444}]Br. The mixture was stirred overnight and ended up with a pale-yellow solution. Subsequently, dichloromethane (CH_2Cl_2) was used to extract [P_{4444}][SS] from the aqueous phase and washed with deionized water to completely remove the impurities. Pure [P_{4444}][SS] was obtained after removing the CH_2Cl_2 through rotary evaporation. The resulting [P_{4444}][SS] was preserved in refrigerator for later uses.

Temperature-dependent UV-vis spectroscopy

Temperature-dependent UV-vis spectroscopy was performed on SHIMADZU UV-3600 with a temperature variation attachment. The molar ratio between [P_{4444}][SS] and H_2O was fixed at 1:300 to specify the LCST around 40 ^oC. The temperature interval was set as 2 ^oC. The proper amount of HCl or NaCl was added to the aqueous solution before the spectroscopic tests when investigating the influence of HCl and NaCl on LCST.

Preparation of HCIS

To prepare HCIS, 1.0 mL of [P_{4444}][SS] was dissolved in 10.0 mL of 10 wt.% gelatin solution. Subsequently, the proper amount of NaCl was mixed with the solution to lower the LCST to a desired region. The concentration of NaCl was fixed at 1.5 $mol \cdot L^-$

[1] for visualizing thermal energy. The mixture was then crosslinked in the presence of 10.0 μL of 20 wt.% glutaraldehyde solution. The crosslinking procedure was conducted under 4 °C for 24 h to guarantee a uniform crosslinking.

^{1}H NMR characterizations

^{1}H NMR spectra were used to verify the mechanism of the phase behavior of [P_{4444}][SS] solution. Constant-temperature ^{1}H NMR spectra were conducted on Bruker 600 MHz spectrometer in D_2O. Temperature-dependent ^{1}H NMR spectra were recorded by JNM-ECA600 spectrometer with D_2O, $CDCl_3$, and DMSO-d6 serving as solvent. The temperature ranged from 25 °C to 60 °C with an interval of 5 °C. The influence of HCl and NaCl on LCST was also investigated through temperature-dependent ^{1}H NMR. The concentrations of HCl and NaCl were 0.2 mol·L^{-1} and 0.9 mol·L^{-1}, respectively. For each sample, the total volume was set as 700.0 μL.

Visualizing thermal distribution through HCIS

For 3D imaging of thermal distribution, a 25.0×25.0×25.0 mm^3 cubic acrylic chamber was fabricated and filled with HCIS. A quartz tube, with an inner diameter of 1.0 mm, went through the middle of the HCIS. Water with the temperatures of 25, 40, 50, and 60 °C were loaded to provide different degrees of thermal energy to HCIS. The 3D thermal distribution was imaged by HCIS timely. Complete thermal information was provided in every direction.

A 5×5 array was fabricated to verify that the HCIS is capable of imaging the sophisticated thermal distribution. Specifically, HCIS was filled into a 35.0×35.0×35.0 mm^3 acrylic chamber with quartz tubes through its body every 5.0 mm both horizontally

and vertically. The quartz tubes were pumped water with different temperatures to perform thermal imaging under complex conditions. Detailed temperature distribution in different tubes is presented in Fig. 5.

Computational simulation

In order to evaluate the heating performance of hydrogel, the temperature distribution of two models of the hydrogel was predicted. In the simulation, the radius, the length, and the wall thickness of the hydrogel are all 25.0 mm or 35.0 mm, and the inside and outside diameters of the capillary tubes are 1.00 mm and 1.05mm, respectively.

After the independence test for gird (Figure S8), it was determined as 74323 element units. In the simulation, all sides of a hydrogel were supposed to be adiabatic. It is assumed that there is only natural convection heat transfer between the model and the environment at the static state, and heat loss from thermal radiation on all surfaces of the hydrogel is considered negligible. The convection heat transfer coefficient was obtained according to the discussion and equations listed below.

The heat exchange in the tube can be considered as single-phase forced convection turbulent heat transfer, and the convection heat transfer coefficient is:

$$h = \frac{Nu_f \lambda}{d} \tag{1}$$

where the thermal conductivity of water (λ) at different temperatures is summarized in Table S1, the inside diameter of the capillary is 1.0 mm. As for the Nusselt number (Nu_f), it is followed by Gnielinski formula:

$$Nu_f = \frac{(f/8)(\mathrm{Re}-1000)\mathrm{Pr}_f}{1+12.7\sqrt{f/8}\left(\mathrm{Pr}_f{}^{2/3}-1\right)} \times \left[1+(d/l)^{2/3}\right] \times c_t \tag{2}$$

$$c_t = \left(\mathrm{Pr}_f / \mathrm{Pr}_w\right)^{0.01} \tag{3}$$

$$\mathrm{Re} = \frac{ud}{v} \tag{4}$$

where the Prandtl number (Pr) and Reynolds number (Re) at different temperatures are shown in Table S2. Therefore, the convective heat transfer coefficient can be calculated 89597, 66750, 49833, 2017 respectively when 0 ^{o}C, 40 ^{o}C, 50 ^{o}C, 60 ^{o}C water are pumped into the capillary.

In the simulation, the close contacts between different materials are taken into consideration, so that thermal contact resistance is neglected. Other thermal-related parameters of the material, including specific heat capacity and thermal conductivity, are obtained from experimental tests or previous literatures. The simulation results show that the distribution of the simulated temperature field is in good agreement with the experimental data

Fire warning system

The fire warning system was fabricated by embedding resistance wires in HCIS and sealed by the transparent acrylic plate. The resistance wires were 25.0 cm long and connected in parallel. The temperature was controlled by varying the current by a direct-current power supply. There are three different states according to the status of HCIS: “Secure”, “Caution” and “Danger”.